Meissner Effect in Colloidal Pb Nanoparticles

Pavlo Zolotavin and Philippe Guyot-Sionnest*

James Franck Institute, The University of Chicago, 929 E. 57th Street, Chicago, Illinois 60637

ABSTRACT Monodisperse colloidal lead nanoparticles with diameters ranging from 4.4 to 20 nm are prepared by a self-limiting growth method. The nanoparticles are monodispersed and protected from oxidation by an amorphous tin—lead oxide shell of 1.5—2 nm thickness. The magnetic susceptibility of the particles is measured as a function of size, temperature, and magnetic field. The Meissner effect is observed indicating the superconducting transition. For the 20 and 16 nm particles, the critical temperature is suppressed to 6.9 K from the bulk value of 7.2 K and is further reduced for smaller particles. Depending on the size of the particles, the critical field is enhanced by 60—140 times. The superconducting properties agree closely with the theoretical expectations.

KEYWORDS: superconductivity · grains · Meissner effect · magnetic susceptibility · critical field · transition temperature · monodisperse · metal nanoparticles · lead · colloidal · oxidation · core—shell

It is an interesting prospect to use nanoscale structuring to modify and possibly improve the superconducting properties of materials. Nanostructure can affect the electronic density[1−4] and the electron−electron and electron−phonon interactions,[5,6] all of which are relevant for superconductors. With advances in colloidal synthesis, increasingly well-monodispersed nanoscale materials can be used to test the superconducting properties of macroscopic samples of nanoparticles with or without interparticle interactions. Considering an individual superconducting grain, the Anderson criterion for superconductivity is that the average spacing between energy levels δ should be comparable or smaller than the superconducting gap Δ.[7] The energy level spacing is inversely proportional to the volume, and this criterion can be fulfilled for Pb when the diameter of the particle is larger than 5 nm.[8] Experimental evidence that superconducting correlations could survive in small particles with $\delta < \Delta$ and are absent for $\delta \geq \Delta$ was made by tunneling through a single superconducting grain,[9,10] while the thermodynamic properties of the granular superconductors were also found to be in agreement with this criterion.[11−13]

Prior experiments on gas-phase deposited Pb particles[14−18] show the evolution of the transition temperature T_C and critical field H_C as expected from theory. Gas-phase preparation of nanoparticles has its drawbacks. In particular, it requires a controlled oxidation to ensure that particles remain isolated from each other, and it does not guarantee that particles are not sintered and that the size distribution of the particles is maintained. More importantly particles prepared in this fashion are restricted to the UHV environment making it difficult for further processing and assembly in superlattices. Monodisperse colloidal particles would bring the ease of the solution-based preparation techniques to the field of granular superconductors. In spite of the benefits that the colloidal nanoparticles can provide, there are few reports on the synthesis of sufficiently small superconducting nanoparticles.[19,20] Previous reports on Pb nanoparticles did not report the Meissner effect at sizes where it should have been expected according to the Anderson criterion. Among the drawbacks of the reported preparation methods is the absence of control over the oxidation.

In this article, we report a synthesis of colloidal core/shell lead particles that alleviates the problems of uncontrolled oxidation. We then report on the magnetic susceptibility of a range of particle sizes and find that the expectations from the Anderson criterion are met.

RESULTS AND DISCUSSION

Synthesis. In developing a new synthesis of colloidal metal nanoparticles starting from metal ions, one usually faces two main

*Address correspondence to pgs@uchicago.edu.

Received for review April 29, 2010 and accepted September 15, 2010.

Published online September 27, 2010.
10.1021/nn102009g

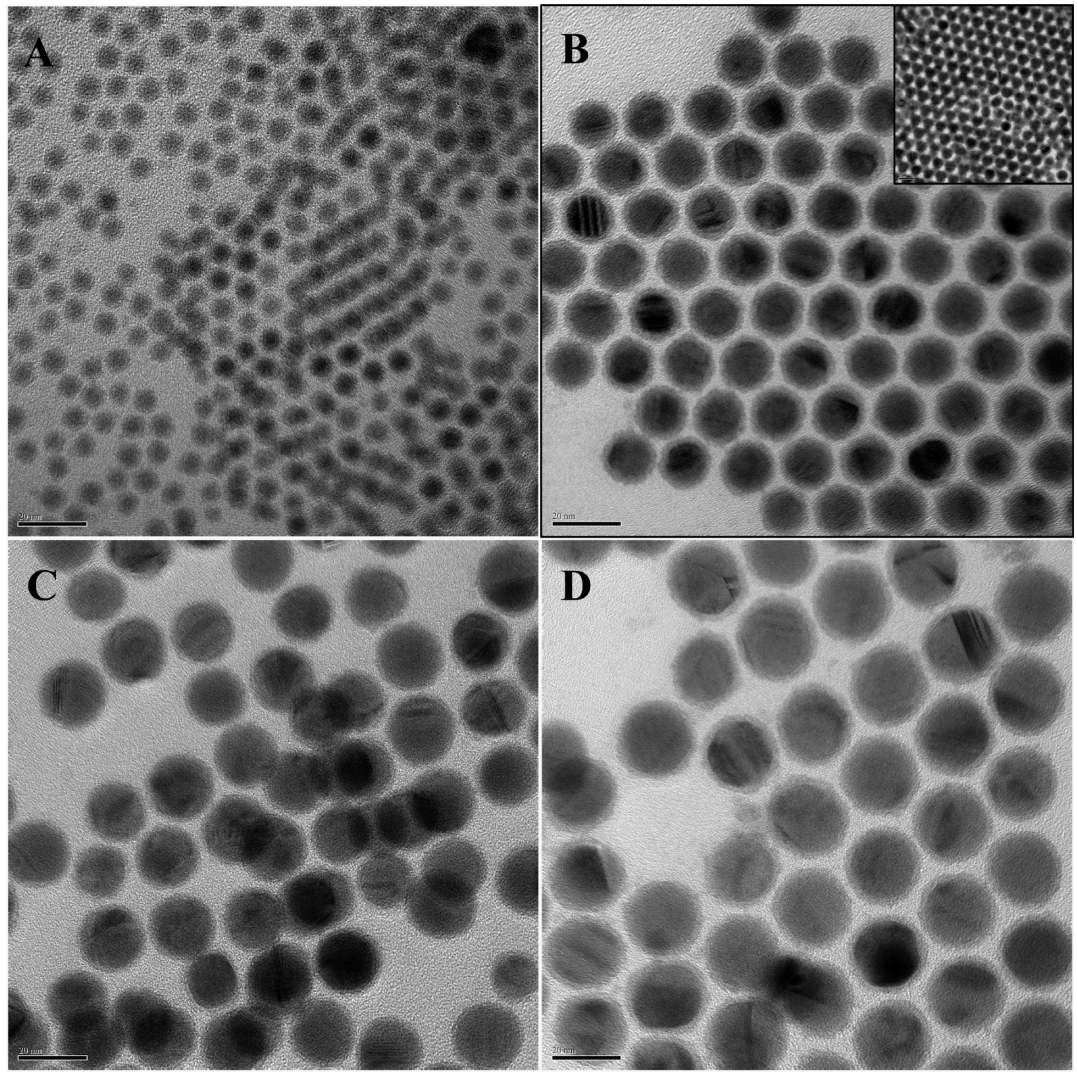

Figure 1. Transmission electron microscopy images of the lead nanoparticles. Core diameters of nanoparticles are (A) 4.4 ± 0.4, (B) 11.4 ± 0.6, (C) 16 ± 1, and (D) 20 ± 1 nm. The shell thickness is in the range of 1.5−2 nm for particles shown. Inset in Figure B shows an example of self-assembly into superlattice. Scale bars in all pictures are 20 nm. TEM pictures for 7.7 ± 0.5 nm nanoparticles are in the SI.

obstacles. The first is finding a suitable reducing agent and the second is stabilizing the surface of the newly formed solid phase. These problems are solved for noble metals and some transition metals with high reduction potentials;[21] however, the successful synthesis of monodispersed metal nanoparticles of the superconducting metals remains scarce.[19,20,22,23] Reduction of the group III and IV elements requires strong reducing agents and in most cases anhydrous conditions. Another complication is that main group metals have low affinity to conventional ligands such as amines and phosphines, or will dissolve upon reacting with thiols or long-chain carboxylic acids. In this work we provide a new synthesis of monodisperse lead nanoparticles in the range from 4 to 20 nm that are protected by a stable oxide shell and that are soluble in organic solvents.

We used a hot injection method to control the nucleation. A tin precursor, $Sn[N(TMS)_2]_2$, was rapidly injected to a solution of lead stearate at 240 °C. The precursor can lead to the formation of elemental lead by two possible reactions. Immediately after the injection a ligand exchange forms $Pb[N(TMS)_2]_2$[24] which then decomposes to provide Pb^0. The tin precursor also decomposes to metallic tin, but at a slower rate. The electrochemical reduction potential of Sn^{2+} is 10 mV smaller than of the Pb^{2+}, thus providing reduction of the Pb^{2+} by metallic tin.

Figure 1 shows TEM images of the lead particles with core diameters from 4 to 20 nm. The largest standard deviation of the particle size distributions is 7%. Nanoparticles typically self-assemble in superlattices on the surface of the TEM grid as shown in the inset of Figure 1. High-resolution TEM images show the crystalline core and an amorphous lower contrast shell that surrounds every particle. Particles are well separated from each other suggesting that they are also well capped by organic ligands that provide solubility in nonpolar solvents. X-ray diffraction spectrum (XRD) of the nanopar-

ticles is shown in Figure 2. Several crystal structures have been reported for lead nanoparticles; however, we see only the cubic face-centered structure of bulk lead.[25] The peak positions agree well with reference data.[26] Peaks are broad due to the small size of the crystals, and in good agreement with the Scherrer formula. The shell on the TEM images is likely an oxide shell, although we did not see a signature of crystalline PbO, SnO, or SnO_2 at the XRD spectra. A fit of the peak at 31.3° shows the presence of a broad low intensity peak at 30.9°, which might be attributed to small inclusions of tetragonal tin.[26] From the nature of the reaction one might assume that the crystalline core of the particles is in fact a lead tin alloy rather than pure lead. Although the positions of the XRD peaks coincide well with the reference data for bulk lead, it does not eliminate the possibility of alloying or inclusions of Sn^0, because the relative concentration of Sn^0 is small.

The EDS spectrum shows the presence of lead and tin (Supporting Information (SI)). Quantitative analysis of the EDS spectra of particles with core diameter of 11 nm gave a tin-to-lead ratio in the range of 0.1−0.15, and for 20 nm particle this ratio decreased to 0.05−0.07. Similar ratios are obtained by elemental analysis: 0.2 and 0.07, respectively. This suggests that tin is more probably located in the shell of the particles.

To determine the oxidation state of the surface atoms we measured high-resolution XPS spectra of the Pb $4f_{7/2}$ and Sn $3d_{5/2}$ bands, which are shown in Figure 3. Survey scan, carbon and oxygen XPS spectra are shown in the SI. The Pb $4f_{7/2}$ band can be fitted with two peaks positioned at 136.5 and 138.5 eV.[27,28] The first peak corresponds to the Pb^0 and the second to the Pb^{2+}. The peak positions and the separation between the Pb $4f_{7/2}$ and Pb $4f_{5/2}$ bands fit the reference data for the native oxides of lead.[29] We also observe a peak at 133.9 eV, but it does not correspond to the reported chemical shifts for the lead compounds. The spectrum of the Sn $3d_{5/2}$ band also shows substructure with a main peak at 486.5 eV, which corresponds to Sn^{2+} and a less intense one for Sn^0 at 484.2 eV. The chemical shifts of SnO and SnO_2 are too close to determine the oxidation state.[26,29] It was reported that complete oxidation of Sn^0 to Sn^{4+} occurs only at elevated temperatures and moist air, and therefore we presume that the oxidized tin is in the Sn^{2+} oxidation state.[30,31] The thickness that is probed by XPS is 5−10 nm and is larger than the combined thickness of ligand and oxide shell (*ca.* 3−3.5 nm). The quantitative analysis of the XPS spectra gives the PbO to SnO ratio as 40% to 60% and Pb^0 to Sn^0 as 54% to 46%. This proportion of Sn is thus much larger than that obtained with elemental analysis and EDS spectra, and therefore supports the notion that tin is concentrated in the shell of the particle. Thus we conclude that most of the tin is in the shell, either as Sn^0 or Sn^{2+}, and arrive at a composition of the shell with SnO, PbO, Sn^0 in the ratio of 50:30:20, respectively.

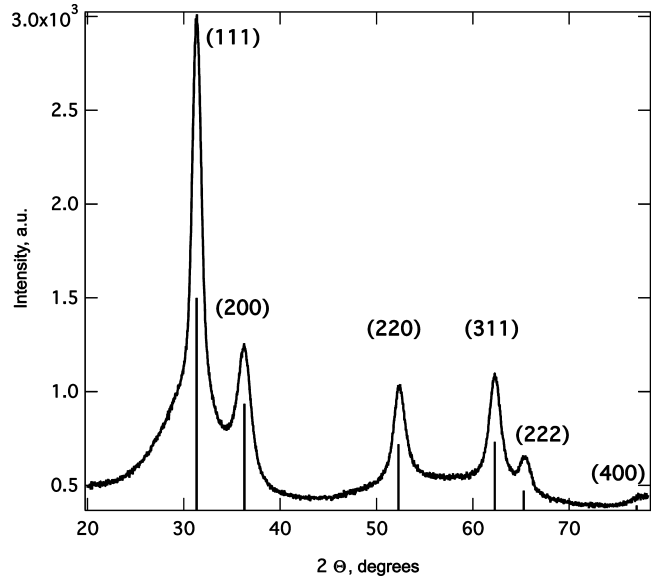

Figure 2. X-ray diffraction spectrum of the 11.4 nm lead nanoparticles. Peak positions and comparison with the reference data can be found in the SI.

We now discuss the origin of the shell. According to published data on oxidation mechanisms of lead tin solders it is primarily tin oxide that is formed on the surface after exposure to air.[32] In attempts to minimize the shell thickness, we performed all the cleaning procedures in inert atmosphere and minimized air exposure before the TEM to 1 min, nevertheless the shell was still present. As a control, we also reproduced a previously published procedure for the preparation of lead nanoparticles using alcohol reduction[20] and, using the same precautions to limit air exposure, we verified that the TEM images showed little or no shell. Therefore we must conclude that the shell is formed during the reaction and is peculiar to the usage of $Sn[N(TMS)_2]_2$ as a reducing agent.

When Sn^0 is oxidized to the Sn^{2+} it forms a salt with the carboxylate group that is left after the reduction of lead stearate. At high temperatures, carboxylate salts of tin have a tendency to decompose to form tin oxide. This process is slow at the growth temperatures and can be accelerated by the presence of amines.[33] The thickness of the shell shows an almost linear growth during the course of reaction (see SI) while the size of the core saturates at 10 nm after 2 min. Meanwhile, the concentration of the particles continues to grow, which we see by the intensification of the color of the solution. We therefore argue that the shell is being formed during the reaction and is not due to the exposure to air. We propose that the amount of SnO formed is small, and that it preferentially nucleates on the particles forming an amorphous oxide shell, rather than making independent nuclei of SnO. A similar reaction is possible for the decomposition of lead stearate that might explain the presence of PbO in the shell; however, the decomposition of lead stearate happens at higher temper-

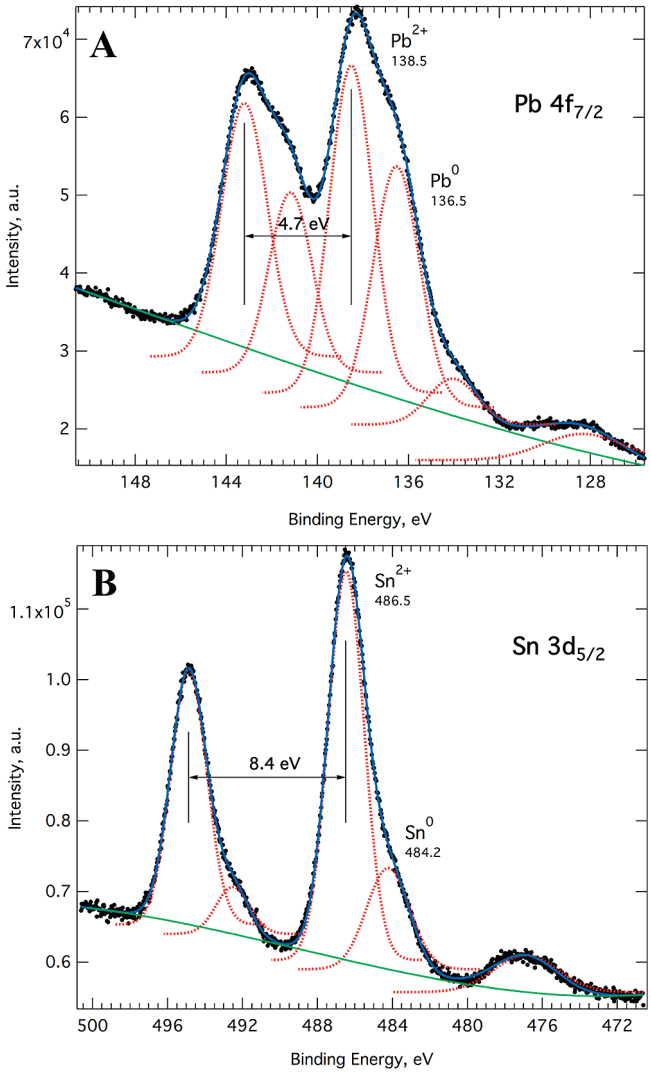

Figure 3. XPS spectrum of a film of lead nanoparticles with core diameter 11.4 nm. Spectra A and B show the Pb $4f_{7/2}$ and Sn $3d_{5/2}$ bands, respectively.

atures than tin stearate,[34] therefore explaining the lower PbO concentration. The unusual saturation of the core growth suggests that the development of the shell slows down the growth and stabilizes the particles at specific sizes. Therefore the growth is self-limiting due to the shell formation. Finally, the long chain carboxylates are weak ligands for metallic lead, and stronger ligand for the tin oxide particles, which explains the high solubility and stability of the colloid.

The presence of the tin oxide shell is thus useful for the formation of the monodisperse colloids. This was tested in an attempt to eliminate the shell by using $Li[N(TMS)_2]$ instead of $Sn[N(TMS)_2]_2$. In this reaction we observed immediate formation of the yellow $Pb[N(TMS)_2]_2$ and its subsequent decomposition to Pb^0. However, the colloids formed did not have a shell and were not very monodisperse, while the reaction yield was low.

The synthesis described above is robust to small variations in the concentrations of lead and tin precursors and produces monodisperse particles with a core diameter of 11 nm. On the basis of the proposed reaction mechanism we developed a variation of the synthesis to make particles with bigger or smaller diameters. The nucleation step and the rate of the shell thickness growth are the key parameters that determine the final size of the particles. Increasing the rate of decomposition of the carboxylic salts will lead to smaller particles and slowing it down will increase the final diameter. The addition of octadecylamine to the initial reaction mixture in 1 to 1 ratio to tin precursor produces particles with a diameter of 4 nm. This observation agrees with the proposed mechanism of the reaction and the fact that amines facilitate the decomposition of carboxylic salts of tin. Decrease of the amine concentration leads to the formation of the bimodal distribution. Changing the length of the chain does not affect the final size. To controll the nucleation step, we exploited the differences in the decomposition rates of the $Pb[N(TMS)_2]_2$ and $Sn[N(TMS)_2]_2$. To prepare the particles with diameter of 7.7 nm, the injection temperature was increased to 285 °C and $Li[N(TMS)_2]$ was added to the tin precursor.

The addition to the reaction mixture of a small amount (5−20 μmol) of indium acetylacetonate leads to the increase in the diameter of the nanoparticles, and the increase of the concentration of In^{3+} leads to the increase of the size of the particles up to 25 nm. A further increase does not affect the size of the particles, but drastically reduces the yield. The final product of the synthesis has however a bimodal distribution. It contains particles with diameters of 4−5 nm and 20 nm. The exact mechanism of this reaction is not known, but one of the possibilities is that In^{3+} provides a side reaction for the formation of the $In[N(TMS)_2]_3$ from the tin precursor leading to a smaller number of nuclei and therefore bigger particles. Lowered reaction yield at high In^{3+} concentration and the presence of small particles favors this assumption, because lowering the tin concentration does not produce similar effects. The other possibility is that the In^{3+} salt modifies the properties of the shell. In support of this suggestion, EDS spectrum and elemental analysis of these particles show the presence of indium. More studies are necessary to elucidate the reason why indium leads to the increase of the particle size and appearance of the bimodal distribution.

The shell that is formed during the reaction serves as an excellent protection from oxidation. Indeed, lead particles without the shell oxidize in 3−5 h when exposed to air. In contrast, when the core/shell particles are exposed to air, Sn^0 in the shell would be the first element to be oxidized therefore decreasing the permittivity for oxygen even further. The nanoparticles with the shell can be handled and stored in air without noticeable change in size distribution for several days. Such particles left on a TEM grid in air for 5 days show an increase in the shell thickness by only 0.5 nm. This

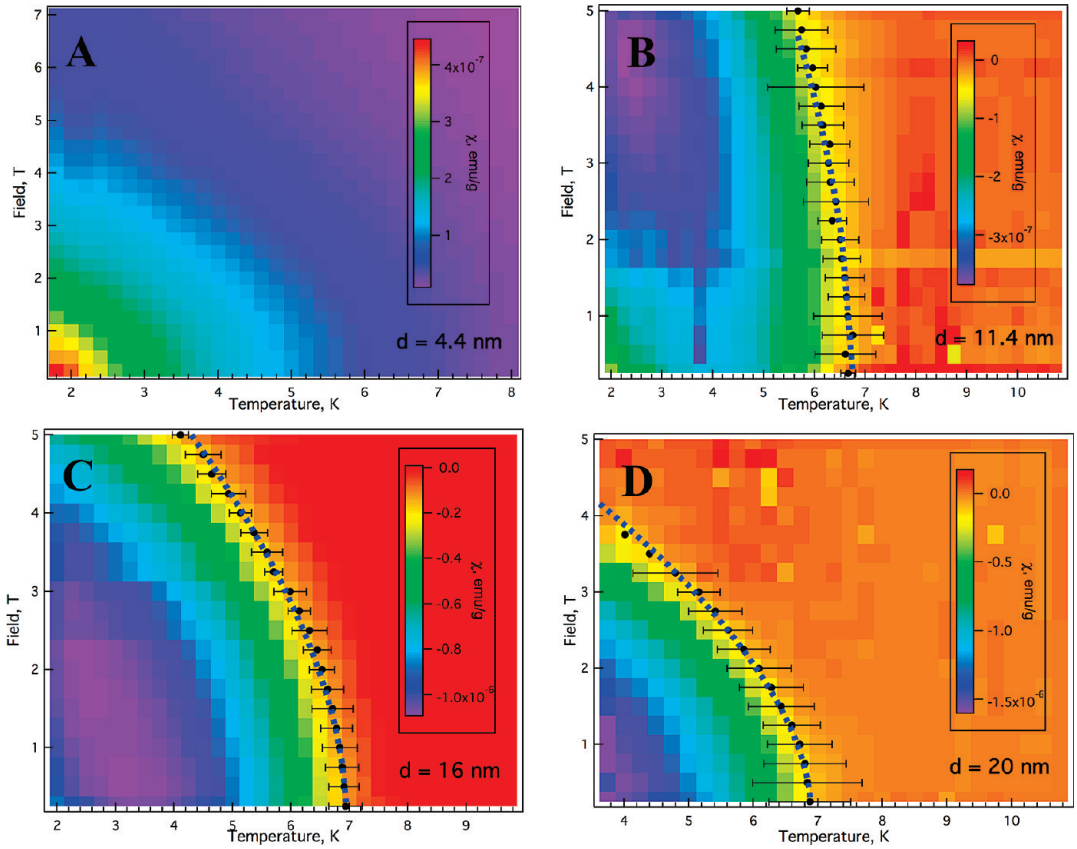

Figure 4. Intensity plots of the magnetic susceptibility as a function of temperature and magnetic field. The color represents the magnitude of the signal, red being high and violet being low. Core diameters of the nanoparticles used for these experiments correspond in the same order to the particles shown on Figure 1 Black dots represent the critical temperature and the blue dashed line separates normal and superconducting phases. Similar data for the nanoparticles with $d = 7.7$ nm are in the SI.

improved stability against oxidation is most helpful to correctly characterize the magnetic superconducting properties of the samples.

Meissner Effect. To characterize the magnetic susceptibility of the nanoparticles, they are precipitated using polar solvents and redispersed in molten paraffin. All the sample processing is performed in the glovebox to minimize oxidation. The NMR quartz tubes are half-filled with paraffin, then the sample is added over a thickness of ~1 cm, and the tube is filled to the top with paraffin to provide further protection from oxidation. This procedure also ensures a uniform background, since as the tube is translated through the pick up coils in the SQUID magnetometer, the only difference in magnetic moment arises from the dissolved lead nanoparticles and the excluded volume of the paraffin.

A color plot of the magnetic susceptibility as a function of temperature and field is shown in Figure 4 for nanoparticles with different diameters. At temperatures higher than T_C the signal is temperature independent and was subtracted as a background. Below the superconducting transition temperature, $T_C(H = 0) = 6.9$ K, the magnetic susceptibility decreases due to the diamagnetic superconducting response. The dashed line is a $H_C(T_C)$ fit that separates the superconducting state from the normal state. The grains are strongly insulated from each other, because the combined thickness of the oxide and ligand shells is 4−5 nm. Therefore, the sample can be viewed as ~10^{15} individual particles in the magnetic field. In a bulk superconductor, the magnetic field is excluded from the entire volume of the sample except for a surface layer of the thickness λ_L, where λ_L is a London penetration length. For lead $\lambda_L = 37$ nm, and therefore the particles studied in this work are completely penetrated by the magnetic field. This brings significant changes to the observed Meissner effect compared with the bulk material.

First, the magnetic susceptibility is much reduced from the bulk value of $\chi^{SC}_{bulk} = -1/(4\pi)$ to

$$\chi^{SC}_{grain} = -\frac{3}{2}\frac{1}{40\pi}\frac{r^2}{\lambda_L^2}\frac{r}{\xi_0} \qquad (1)$$

where r is the radius of the particle, ξ_0 is the coherence length, and λ_L is the London penetration depth.[35,36] For lead particles of 11.4 nm diameter this leads to the reduction in the signal amplitude by 5.3×10^4 times. Combining this fact with the milligram quantities obtained in one reaction batch makes it a challenging measurement. It may be one of the reasons why the Meissner effect at

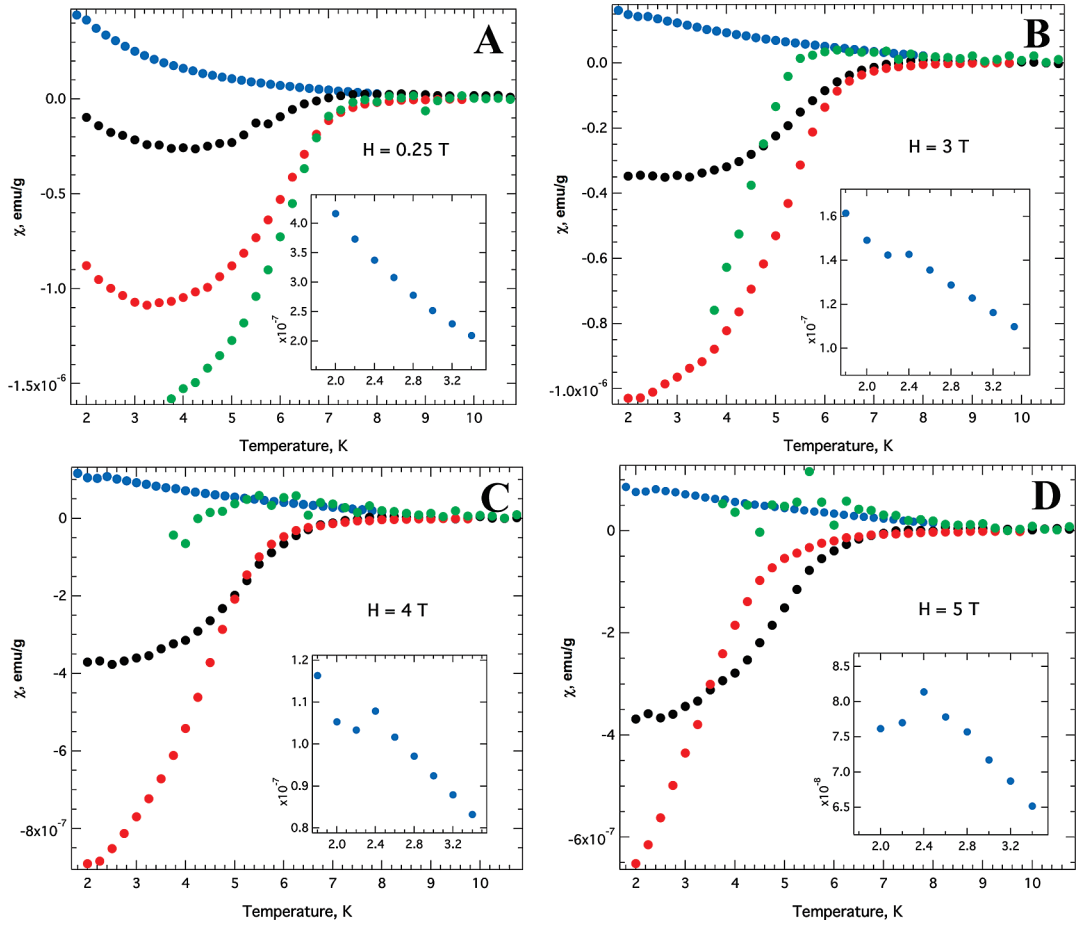

Figure 5. Magnetic susceptibility as a function of temperature measured at magnetic fields of 0.25 (A), 3(B), 4(C), and 5 T (D). The color of the traces corresponds to different sizes of the nanoparticles: (blue) 4.4, (black) 11.4, (red) 16, and (green) 20 nm. Inset is a magnification of the graph for 4.4 nm particles at low temperatures.

small sizes has not been previously reported. The high reproducibility of the synthesis allowed combining several batches of nanoparticles in order to achieve a stronger signal. For particles of 11 nm and larger, the agreement of the observed susceptibility with theoretical expectation is good. The amplitude of the signal for the 4 nm diameter particles is smaller than expected by 11 times, but the dependence on the diameter is still in fair agreement with the theoretical prediction, see SI. Thus the observed small negative deviation from the otherwise Curie law in the signal for 4 nm particles is also assigned to the superconducting transition.

For the critical temperature determination in a bulk superconductor, $\chi^{SC}(T)$ is a step function with a transition width determined by crystal imperfections.[35] For nanoparticles, $\chi(T)$ curves are smooth as shown on the Figure 5. According to eq 1 the magnetic susceptibility is $\chi^{SC}_{grain} \approx \lambda_L^{-2}$ with $\lambda_L(t) \approx (1 - t^4)^{-1/2}$, where $t = T/T_C$. The signal below T_C is thus proportional to the fourth power of temperature. The effect of the fluctuation in the order parameter is another feature of the superconducting transition in small particles. This can be observed as an onset of the diamagnetism above the transition temperature. Following a literature procedure, the critical temperature at varying magnetic field, $T_C(H)$, was then chosen as the intersection of the T^4 fit of the $\chi(T)$ with the horizontal line.[37] Example of this procedure and the London equation fit[38,39] are shown in the SI. For high magnetic fields for 16 and 20 nm diameter particles, T_C is close to the lower accessible temperature, thus making this procedure impossible. For these points T_C was then estimated as the onset of the negative diamagnetic contribution.

Along with the Meissner effect we also observe a temperature dependent paramagnetic contribution, Figure 4 and 5. For 4.4 nm particles this is the major contribution to the magnetic susceptibility, and for bigger particles it is observed at low values of the magnetic field and temperature. If the number of electrons in the isolated metal nanoparticle is odd, then the unpaired electron will provide a re-entrant Curie-like contribution to the magnetic susceptibility.[8,40,41] This can be observed only for metal nanoparticles when kT is much smaller than the level spacing. However, the paramagnetic signal is not due to the odd/even effects, because we do not see a $\sim d^{-3}$ scaling with diameter of the particles.[36] A closer look at Figure 5 reveals that the magnetic susceptibility curves for the 4 nm particles and 20 nm particles coincide at H = 5 T when the superconducting response of the bigger particles is completely

suppressed. The absolute intensity of the signal corresponds to ~10 spins per particle. These observations suggest that this paramagnetic response is a contamination of the starting materials by paramagnetic impurities, or results from the nonstoichiometric sites in the oxide shell.

Figure 6 shows the critical temperature as a function of magnetic field. The magnetic behavior of the small particles is analogous to that for thin superconducting film in the parallel field geometry. In both cases, the entire volume of the sample is penetrated by the magnetic field and the superconducting transition becomes first order. Therefore, instead of using an empirical law $H_C(t) \approx (1 - t^2)$ that is widely used for bulk materials, we can use

$$H_C(t) = H_C(0)\sqrt{1 - t} \qquad (2)$$

which is suggested for small spherical grains.[43] Another option is to use an implicit condition for the critical field and temperature:

$$\ln \frac{T_C(H)}{T_C(0)} = \Psi\left(\frac{1}{2}\right) - \Psi\left(\frac{1}{2} + \frac{\hbar}{4\pi k_B T_C(H)\tau_K}\right) \qquad (3)$$

where

$$\frac{1}{\tau_K} = 1.76 k_B T_c(0)\left[\frac{H_c(T)}{H_c(0)}\right]^2 \qquad (4)$$

and Ψ is a digamma function.[42,43] Both function are plotted in Figure 6 together with experimental data for 7.7, 11.4, 16, and 20 nm particles. Results of the fit are summarized in Table 1 and also plotted on the insets of the Figure 6 as a function of the diameter of the particles. For the theoretical values of the critical field we use $H_C = 4.85(\lambda_L\xi_0^{1/2}/R^{3/2})H_{C,\,bulk}$, where $H_{C,\,bulk} = 0.08$ T is the bulk value of the critical field.[44] Our experimental values of the critical field are 1.3−1.4 times larger than the theoretical predictions; however, the dependence on the size of the particles is well maintained. Previous experiments in gas-phase condensed Pb particles systems[11] report values of the critical field that are about 2 times smaller than what is reported here. A partial sintering of the unprotected particles as described in ref 11 is a possible explanation for the discrepancy between the two preparations. Depending on the initial theoretical assumptions there are several variants for the prefactor in the formula for the critical field, but all of them are smaller than used above,[45] so this is not improving the agreement. As an alternative explanation, we note that the effective radius that will provide agreement between theory and experiment is about one standard deviation smaller than the average size. This small deviation from theory could then be explained by a decrease in size of the particles due to oxidation; however, the systematic nature of the deviation rules this out. Our preferred reason for the small deviation lies in the nature of the surface scattering and the

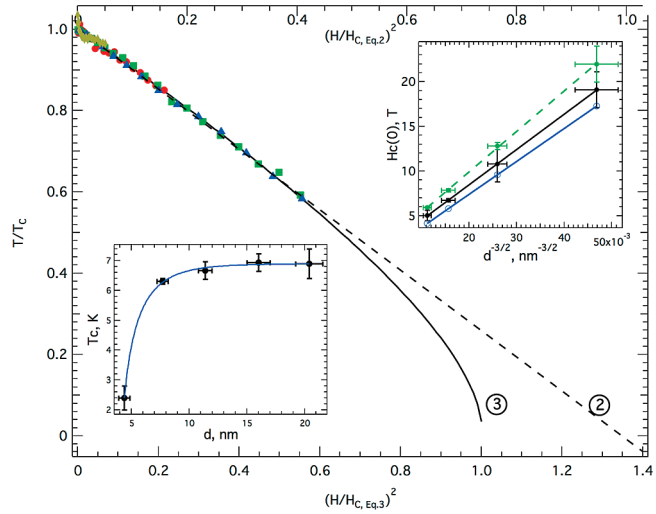

Figure 6. Transition temperatures for particles of 20 (triangles), 16 (squares), 11.4 (circles) and 7.7 (diamonds) as a function of the applied magnetic field. The dashed and solid black lines correspond to eq 2 (top axis) and eq 3 (bottom axis), respectively. Right inset: Critical field as a function of particle size. Fits are shown, dashed green line with eq 2, and black line with eq 3. The blue line is the expectation from theory. Left inset: Critical temperature as a function of particle size. The blue line is a guide to the eye.

τ_k^{-1} term. It seems likely that the surface should show an effect on the magnetic response and that this can only be seen with small, monodispersed, and stable superconducting systems as synthesized here.

The critical temperature of bulk lead is 7.2 K. For particles with diameters 16 and 20 nm we observe a slight depression of $T_C = 6.9$ K. Qualitatively it could be explained by several reasons. The observed paramagnetic contribution arises from unpaired spins that have a pair breaking effect, therefore lowering the T_C. Also, softer surface phonons could enhance the T_C for the free-lead surface, while in the case of the oxide-covered particles, the phonon spectrum should be affected in the opposite way.[5]

Particles with diameter 11.4 nm show a further decrease in the critical temperature to $T_C = 6.7$ K. For this size, the ratio of the average level spacing to the superconducting energy gap is $\delta/\Delta \approx 0.1$ and the discreteness of the energy levels begins to play role. The decrease of the critical temperature continues for the 7.7 nm particles with $T_C = 6.3$ K. The critical ratio δ/Δ at which superconductivity disappears is predicted to be different for par-

TABLE 1. Summary of the Fit of the Experimental Data to eq 2 and eq 3, Compared to the Theoretically Predicted Values of the Critical Magnetic Field. δ/Δ is a Ratio of the Average Level Spacing to the Superconducting Energy Gap

d, nm	δ/Δ	T_C^{Exper}, K	$H_C^{Exp.\ Eq.2}$, T	$H_C^{Exp.\ Eq.3}$, T	H_C^{Theory}, T
20 ± 1	0.02	6.9 ± 0.5	5.9 ± 0.1	5.0 ± 0.6	4.2
16 ± 1	0.03	6.9 ± 0.3	7.8 ± 0.2	6.7 ± 0.2	5.8
11.4 ± 0.6	0.09	6.7 ± 0.3	12.8 ± 0.4	11 ± 2	9.6
7.7 ± 0.5	0.3	6.3 ± 0.1	22 ± 2	19 ± 2	17
4.4 ± 0.4	1.6	2.4 ± 0.4	-	-	40

ticles with odd and even number of electrons and is 0.89 and 3.56, respectively.[46] The smallest particles of diameter 4.4 nm show $T_C = 2.4$ K. This result is a direct consequence of the finite level spacing as for this size $\delta/\Delta \approx 1.6$ and is in qualitative agreement with theoretical calculations. The size dependence of the critical temperature follows closely that measured before for gas-condensed particles.[11] The abrupt change in the critical temperature in the range from 4 to 6 nm echos the sudden change in the superconducting gap that was also observed for single islands of lead.[4]

In summary, we have developed a new procedure for the preparation of colloidal monodisperse lead particles that are much less prone to oxidation than in previous studies. This allowed the first measurement of the magnetic susceptibility on superconducting colloidal nanoparticles down to very small sizes where T_C is affected. The superconducting state is present in Pb colloidal nanoparticles as small as 4.4 nm albeit with a strongly depressed T_C. The results are in good agreement with the Anderson criterion and prior experiments on gas-phase condensed nanoparticles, although the critical field is measured to be ~2-fold larger for the colloidal particles. This work adds colloidal superconducting nanoparticles to the toolkit for the nanoengineering of future materials.

METHODS

Lead stearate was purchased from Chem Service; all other materials were from Sigma-Aldrich and used as received without purification. Solvents were of the anhydrous grade, and all the procedures were made in a Schlenk line or in a glovebox with nitrogen atmosphere.

A procedure for the preparation of particles with a lead core of 11 nm diameter and 1.7 nm shell thickness was as follows. In 6 mL of 1-octadecene, 70 mg of lead stearate (90 μmol) and 0.05 mL of trioctylphosphine (110 μmol) were dissolved. The quality of the lead precursor is a crucial component to make a preparation procedure reproducible. An excess of the carboxylic acid that is not converted to the lead salts is of the greatest concern. The reaction mixture was kept under vacuum in the Schlenk line for 30 min at room temperature and then for 15 min at 100 °C, periodically flushing the flask with argon. Under argon the temperature was increased to 244 °C and 1.1 mL of 0.06 M solution of bis[bis(trimethylsilyl)amino]tin(II), $Sn[N(TMS)_2]_2$, in hexadecane was rapidly injected. The temperature of the reaction mixture instantaneously drops to 210 °C and then jumps back to 218−220 °C at which it was stabilized. After the injection the color of the solution turns black within several seconds, which indicates nucleation and growth of the lead particles. The solution was kept at 220 °C for 6−7 min and then was cooled down to room temperature. It was then degassed to remove volatile products and transferred to the glovebox for cleaning.

Nanoparticles were centrifuged after precipitation with 2-propanol/ethanol mixture. The supernatant was decanted and the precipitate was redissolved in toluene or hexane. The cleaning procedure was repeated two more times using pure 2-propanol for the precipitation. After the last cleaning cycle, particles were redissolved in hexane and the excess of lead stearate was filtered trough a 0.2 μm Millipore filter. Transmission electron microscopy images of the filtered and unfiltered solutions did not show a significant change in the particle size distribution. Filtered particles form a stable colloid and could be stored under argon for 1−2 months. Particles could also be cleaned and stored in air; however, in this case the shelf life is limited to several weeks. To ensure complete cleaning, the nanoparticles were precipitated several more times before conducting measurements. This step lowers the colloid stability and was performed right before the experiments. The weight of the cleaned nanoparticles is 10−12 mg, which corresponds to ~50% final yield. The synthesis can be scaled up to 10 times without loosing the monodisperse size distribution.

To decrease the size of the particles, $Li[N(TMS)_2]$ was added to the tin precursor. Increase of the $Li[N(TMS)_2]$ concentration leads to the decrease in the diameter of the particles. For the preparation of the particles with diameter of 7.7 nm the following conditions were used. A 840 mg portion of lead stearate was dissolved in 8 mL of 1-octadecene and degassed for 1 h at room temperature and then filled with argon. Injection solution was mixed in the glovebox from a 0.4 mL of $Sn[N(TMS)_2]_2$, 0.1 mL of trioctylphosphine, 1 mL of 0.1 M solution of $Li[N(TMS)_2]$ in hexadecane and 2.2 mL of hexadecane. After injection at 285 °C temperature was stabilized at 220 °C and kept for 4 min. Cleaning procedures were the same as for 4.4 nm nanoparticles.

Particles with core diameters larger than 10 nm were prepared with addition of the indium acetylacetonate to the reaction mixture. The size of the particles can be controlled by changing the initial concentration of TOP and indium salt. An increase of the In^{3+} concentration leads to the increase of the nanoparticle diameter. Changes in the TOP concentration have an opposite effect. For the final tuning of the core size in the range of several nanometers the concentration of the tin precursor can be adjusted in the range of 0.055−0.065 M. For example for the synthesis of 20 nm particles, the reaction conditions were changed in the following way. A 3.5 mg portion of indium acetylacetonate (8 μmol), 0.03 mL of TOP (65 μmol), and 230 mg of lead stearate (300 μmol) were added to 17 mL of ODE. The volume of the injected tin precursor was increased to 3.6 mL. When In^{3+} ions are present, the resulting colloid has a bimodal distribution of particles with diameters of 20 nm and 4−5 nm. The fraction of smaller particles can be easily removed by size-selective precipitation with 2-propanol. All other procedures remained unchanged.

To prepare particles with smaller core diameters of ~4 nm, octadecylamine (ODA) was added to the initial reaction mixture in the ratio 0.9:1 to the tin precursor. Better results were obtained if TOP was not added. The product of this reaction contains a fraction of particles of larger diameters. These particles can be removed by size selective precipitation. For this size of particles, the reaction byproducts can be effectively cleaned by centrifugation of the hexane solution of nanoparticles after the first precipitation cycle. All other procedures remained unchanged.

The transmission electron images (TEM) were obtained at 300 kV using an FEI Tecnai F30, equipped with energy dispersive X-ray spectrometer (EDS) for compositional analysis. A drop of dilute solution of nanoparticles was allowed to dry on the TEM grid in the inert atmosphere and transferred to the TEM in a closed vial. Exposure to air was limited to a few minutes. Size distributions were measured manually using the ImageJ program on at least 100 particles. The diffraction patterns were collected using a Bruker D8 diffractometer with Cu Kα X-ray source operating at 40 kV and 40 mA and Vantec 2000 area detector.

Low-resolution X-ray photoelectron spectroscopy (XPS) measurements were performed in the Keck Interdisciplinary Surface Science (Keck-II) facility of Northwestern University using an Omicron ESCA Probe system. High-resolution XPS spectra were acquired with a Phoibos HSA 3500 Energy Analyzer. Samples for the XPS were prepared by drying of the concentrated colloids on the silicon substrate in the inert atmosphere. Elemental analysis of the 11.4 and 20 nm particles was performed by Galbraith Laboratories, Inc.

Measurements of the magnetic susceptibility of 11.4 and 20 nm particles were performed using a Quantum Design MPMS and for 4.4 and 16 nm particles using the MPMS-XL in the Center for Nanoscale Materials of Argonne National Laboratory. Mag-

netic susceptibility is reported in emu units per gram of lead in the core of the particles, which was estimated on the basis of the spherical geometry and total sample weight. Several batches of particles were combined into one sample after checking that their average sizes were within ±0.5 nm. The dry weights of the samples used for SQUID measurements ranged from 30 to 100 mg. Particles were dissolved in a previously degassed wax and positioned in the EPR tube of the 4 mm diameter half filled with wax. From the top, particles were sealed with the same wax. This arrangement provides an almost background free measurement and also further excellent protection from oxidation. Measurements were done in field-cooled mode, scanning the field at each temperature point. No difference in signal intensity was observed for zero-field-cooled and field-cooled experiments suggesting that there is no coupling between particles due to the thick oxide and ligand shell.

Acknowledgment. We thank Dr. Maksym Kovalenko for the discussion of the mechanism of reaction and taking an XRD spectrum, Miki Nakayama for the XPS data, Dr. Herve Aubin for helpful discussions, and Prof. Thomas Rosenbaum for sharing the SQUID magnetometer. Use of the SQUID magnetometer at the Center for Nanoscale Materials was supported by the U.S. Department of Energy, Office of Science, Office of Basic Energy Sciences, under Contract No. DE-AC02-06CH11357. The work was supported by the University of Chicago MRSEC NSF-DMR under Grant No. DMR-0213745.

Supporting Information Available: Additional material characterization data: TEM images, XPS and EDX spectra, XRD and XPS peak positions, time evolution of the core diameter and shell thickness; intensity plots of the magnetic susceptibility as a function of temperature and magnetic field for particles with core diameter of 7.7 nm; examples of the fitting procedures used to extract critical temperature. This material is available free of charge *via* the Internet at http://pubs.acs.org.

REFERENCES AND NOTES

1. Guo, Y.; Zhang, Y. F.; Bao, X. Y.; Han, T. Z.; Tang, Z.; Zhang, L. X.; Zhu, W. G.; Wang, E. G.; Niu, Q.; Qiu, Z. Q.; *et al.* Superconductivity Modulated by Quantum Size Effects. *Science* **2004**, *306*, 1915–1917.
2. Qin, S. Y.; Kim, J.; Niu, Q.; Shih, C. K. Superconductivity at the Two-Dimensional Limit. *Science* **2009**, *324*, 1314–1317.
3. Shanenko, A. A.; Croitoru, M. D.; Peeters, F. M. Quantum-Size Effects on T_c in Superconducting Nanofilms. *Europhys. Lett.* **2006**, *76*, 498–504.
4. Bose, S.; Garcia-Garcia, A. M.; Ugeda, M. M.; Urbina, J. D.; Michaelis, C. H.; Brihuega, I.; Kern, K. Observation of Shell Effects in Superconducting Nanoparticles of Sn. *Nat. Mater.* **2010**, *9*, 550–554.
5. Matsuo, S.; Sugiura, H.; Noguchi, S. Superconducting Transition-Temperature of Aluminum, Indium, and Lead Fine Particles. *J. Low Temp. Phys.* **1974**, *15*, 481–490.
6. Aliev, A. E.; Lee, S. B.; Zakhidov, A. A.; Baughman, R. H. Superconductivity in Pb Inverse Opal. *Phys. C (Amsterdam)* **2007**, *453*, 15–23.
7. Anderson, P. W. Theory of Dirty Superconductors. *J. Phys. Chem. Solids* **1959**, *11*, 26–30.
8. Kubo, R.; Kawabata, A.; Kobayashi, S. Electronic-Properties of Small Particles. *Annu. Rev. Mater. Sci.* **1984**, *14*, 49–66.
9. von Delft, J.; Ralph, D. C. Spectroscopy of Discrete Energy Levels in Ultrasmall Metallic Grains. *Phys. Rep.* **2001**, *345*, 61–173.
10. Tinkham, M.; Ralph, D. C.; Black, C. T.; Hergenrother, J. M. Discrete Energy Levels and Superconductivity in Nanometer-Scale Al Particles. *Czech. J. Phys.* **1996**, *46*, 3139–3145.
11. Li, W. H.; Yang, C. C.; Tsao, F. C.; Lee, K. C. Quantum Size Effects on the Superconducting Parameters of Zero-Dimensional Pb Nanoparticles. *Phys. Rev. B* **2003**, *68*, 184507–184513.
12. Wu, F. Y.; Yang, C. C.; Wu, C. M.; Wang, C. W.; Li, W. H. Superconductivity in Zero-Dimensional Indium Nanoparticles. *J. Appl. Phys.* **2007**, *101*, 09G111−09G114.
13. Cuppens, J.; Romero, C. P.; Lievens, P.; Van Bael, M. J. Superconductivity in Pb Cluster Assembled Systems with Different Degrees of Coagulation. *Phys. Rev. B* **2010**, *81*, 064517−064524.
14. Perenboom, J. A. A. J.; Wyder, P.; Meier, F. Magnetic-Properties of Samples Containing Small Indium Particles. *Phys. Rev. B* **1981**, *23*, 279–286.
15. Hindley, N. K.; Watson, J. H. P. Superconducting Metals in Porous Glass as Granular Superconductors. *Phys. Rev.* **1969**, *183*, 525–528.
16. Bernardi, E.; Lascialfari, A.; Rigamonti, A.; Romano, L.; Iannotti, V.; Ausanio, G.; Luponio, C. Zero-Dimensional Superconducting Fluctuations and Fluctuating Diamagnetism in Lead Nanoparticles. *Phys. Rev. B* **2006**, *74*, 134509–134517.
17. Fariss, T. L.; Nixon, W. E.; Bucelot, T. J.; Deaver, B. S.; Mitchell, J. W. Superconducting Lead Particles Produced by Chemical Techniques. *J. Appl. Phys.* **1982**, *53*, 6316–6324.
18. Reich, S.; Leitus, G.; Popovitz-Biro, R.; Schechter, M. Magnetization of Small Lead Particles. *Phys. Rev. Lett.* **2003**, *91*, 147001–147005.
19. Weitz, I. S.; Sample, J. L.; Ries, R.; Spain, E. M.; Heath, J. R. Josephson Coupled Quantum Dot Artificial Solids. *J. Phys. Chem. B* **2000**, *104*, 4288–4291.
20. Resa, I.; Moreira, H.; Bresson, B.; Mahler, B.; Dubertret, B.; Aubin, H. Synthesis of Monodisperse Superconducting Lead Nanocrystals. *J. Phys. Chem. C* **2009**, *113*, 7120–7122.
21. Burda, C.; Chen, X. B.; Narayanan, R.; El-Sayed, M. A. Chemistry and Properties of Nanocrystals of Different Shapes. *Chem. Rev.* **2005**, *105*, 1025–1102.
22. Chou, N. H.; Ke, X. L.; Schiffer, P.; Schaak, R. E. Room-Temperature Chemical Synthesis of Shape-Controlled Indium Nanoparticles. *J. Am. Chem. Soc.* **2008**, *130*, 8140–8141.
23. Soulantica, K.; Maisonnat, A.; Fromen, M. C.; Casanove, M. J.; Lecante, P.; Chaudret, B. Synthesis and Self-Assembly of Monodisperse Indium Nanoparticles Prepared from the Organometallic Precursor [In(η^5-C_5H_5)]. *Angew. Chem., Int. Ed.* **2001**, *40*, 448–451.
24. Gynane, M. J. S.; Harris, D. H.; Lappert, M. F.; Power, P. P.; Riviere, P.; Rivierebaudet, M. Subvalent Group-4B Metal Alkyls and Amides. Part 5. The Synthesis and Physical Properties of Thermally Stable Amides of Germanium(II), Tin(II), and Lead(II). *J. Chem. Soc., Dalton Trans.* **1977**, 2004–2009.
25. Wu, Y.; Chen, Q.; Takeguchi, M.; Furuya, K. High-Resolution Transmission Electron Microscopy Study on the Anomalous Structure of Lead Nanoparticles with UHV-MBE-TEM System. *Surf. Sci.* **2000**, *462*, 203–210.
26. Joint Committee on Powder Diffraction Standards. *Selected Powder Diffraction Data for Minerals*, 1st ed.; American Society for Testing and Materials: Swarthmore, Pa, 1974.
27. Wagner, C. D., *Handbook of X-Ray Photoelectron Spectroscopy: A Reference Book of Standard Data for Use in X-Ray Photoelectron Spectroscopy*; Physical Electronics Division Perkin Elmer Corp.: Eden Prairie, Minn., 1979; pp 118−119, 160−161.
28. Khanuja, M.; Kala, S.; Mehta, B. R.; Sharma, H.; Shivaprasad, S. M.; Balamurgan, B.; Maisels, A.; Kruis, F. E. XPS and AFM Studies of Monodispersed Pb/PbO Core−Shell Nanostructures. *J. Nanosci. Nanotechnol.* **2007**, *7*, 2096–2100.
29. Crist, B. V. *Handbook of Monochromatic XPS Spectra*. Wiley: Chichester, New York, 2000; pp 202−204, 423−425, 259−261, 471−473.
30. Batzill, M.; Diebold, U. The Surface and Materials Science of Tin Oxide. *Prog. Surf. Sci.* **2005**, *79*, 47–154.
31. Domashevskaya, E. P.; Ryabtsev, S. V.; Turishchev, S. Y.; Kashkarov, V. M.; Yurakov, Y. A.; Chuvenkova, O. A.; Shchukarev, A. V. XPS and XANES Studies of SnO_x Nanolayers. *J. Struct. Chem.* **2008**, *49*, S80–S91.
32. Konetzki, R. A.; Chang, Y. A.; Marcotte, V. C. Oxidation-Kinetics of Pb-Sn Alloys. *J. Mater. Res.* **1989**, *4*, 1421–1426.

33. Epifani, M.; Arbiol, J.; Diaz, R.; Peralvarez, M. J.; Siciliano, P.; Morante, J. R. Synthesis of SnO_2 and ZnO Colloidal Nanocrystals from the Decomposition of Tin(II) 2-Ethylhexanoate and Zinc(II) 2-Ethylhexanoate. *Chem. Mater.* **2005**, *17*, 6468–6472.
34. Mohamed, M. A.; Halawy, S. A.; Ebrahim, M. M. Nonisothermal Kinetic and Thermodynamic Study of the Decomposition of Lead Acetate Trihydrate. *Thermochim. Acta* **1994**, *236*, 249–262.
35. Tinkham, M. *Introduction to Superconductivity*, 2nd ed.; McGraw Hill: New York, 1996.
36. Denton, R.; Muhlschl, B.; Scalapino, D. J. Thermodynamic Properties of Electrons in Small Metal Particles. *Phys. Rev. B* **1973**, *7*, 3589–3607.
37. Buhrman, R. A.; Halperin, W. P. Fluctuation Diamagnetism in a Zero-Dimensional Superconductor. *Phys. Rev. Lett.* **1973**, *30*, 692–695.
38. von London, F. Zur Theorie Magnetischer Felder Im Supraleiter. *Physica* **1936**, *3*, 450–462.
39. Muhlschl, B.; Scalapin, D. J.; Denton, R. Thermodynamic Properties of Small Superconducting Particles. *Phys. Rev. B* **1972**, *6*, 1767–1777.
40. Di Lorenzo, A.; Fazio, R.; Hekking, F. W. J.; Falci, G.; Mastellone, A.; Giaquinta, G. Re-entrant Spin Susceptibility of a Superconducting Grain. *Phys. Rev. Lett.* **2000**, *84*, 550–553.
41. Halperin, W. P. Quantum Size Effects in Metal Particles. *Rev. Mod. Phys.* **1986**, *58*, 533–606.
42. de Gennes, P. G.; Tinkham, M. Magnetic Behavior of Very Small Superconducting Particles. *Physics* **1964**, *1*, 107–126.
43. Hurault, J. P.; Maki, K.; Beal-Monod, M. T. Fluctuations of Order Parameter in Small Superconducting Samples. *Phys. Rev. B* **1971**, *3*, 762–768.
44. Lide, D. R. *CRC Handbook of Chemistry and Physics: A Ready-Reference Book of Chemical and Physical Data*, 90th ed.; Lide., D. R., Ed.; CRC: Boca Raton, Fl, 2009.
45. Perenboom, J. A. A. J.; Wyder, P.; Meier, F. Electronic-Properties of Small Metallic Particles. *Phys. Rep.* **1981**, *78*, 173–292.
46. von Delft, J.; Zaikin, A. D.; Golubev, D. S.; Tichy, W. Parity-Affected Superconductivity in Ultrasmall Metallic Grains. *Phys. Rev. Lett.* **1996**, *77*, 3189–3192.